Evaluation of Nanoparticle Tracking for Characterization of Fibrillar Protein Aggregates

Dennis T. Yang
Dept. of Chemical and Biological Engineering, University of Wisconsin, Madison, WI 53706

Xiaomeng Lu
Biophysics Program, University of Wisconsin, Madison, WI 53706

Yamin Fan
Dept. of Chemical and Biological Engineering, Zhejiang University, Hangzhou, Zhejiang, P.R. China

Regina M. Murphy
Dept. of Chemical and Biological Engineering, University of Wisconsin, Madison, WI 53706

DOI 10.1002/aic.14349
Published online January 28, 2014 in Wiley Online Library (wileyonlinelibrary.com)

Amyloidogenesis is the process of formation of protein aggregates with fibrillar morphology. Because amyloidogenesis is linked to neurodegenerative disease, there is interest in understanding the mechanism of fibril growth. Kinetic models of amyloidogenesis require data on the number concentration and size distribution of aggregates, but this information is difficult to obtain using conventional methods. Nanoparticle tracking analysis (NTA) is a relatively new technique that may be uniquely suited for obtaining these data. In NTA, the two-dimensional (2-D) trajectory of individual particles is tracked, from which the diffusion coefficient, and, hence, hydrodynamic radius is obtained. Here we examine the validity of NTA in tracking number concentration and size of DNA, as a model of a fibrillar macromolecule. We use NTA to examine three amyloidogenic materials: beta-amyloid, transthyretin, and polyglutamine-containing peptides. Our results are instructive in demonstrating the advantages and some limitations of single-particle diffusion measurements for investigating aggregation in protein systems. © 2014 American Institute of Chemical Engineers *AIChE J*, 60: 1236–1244, 2014
Keywords: nanoparticle tracking, amyloid, fibrils, protein aggregation, DNA

Introduction

Protein aggregation is an important problem for both biomanufacturing and clinical disease. Of particular current interest are proteins that self-assemble into amyloid fibrils. These large protein aggregates have cross-β sheet structure and fibril morphology; typical fibrils are ~5–10 nm in diameter and ~200 nm - 1 μm or more in length. Deposition of amyloid fibrils in tissues is associated with a diverse array of degenerative disorders. The direct link between fibril formation and disease has motivated efforts to investigate the structure of fibrils, the pathway by which native proteins convert to fibrils, the kinetics of fibril formation and growth, and the relationship between aggregation and cellular toxicity.[1–4]

Three examples of amyloidogenic proteins are transthyretin, beta-amyloid, and huntingtin. Transthyretin (TTR) is a homotetrameric transport protein, abundant in both blood and cerebrospinal fluid. TTR aggregation into fibrils is the basis of several disorders including senile systemic amyloidosis[5] and familial amyloid polyneuropathy.[6] Beta-amyloid (Aβ) aggregation is causally associated with Alzheimer's disease. Aβ is a short (4 kDa) peptide produced by proteolytic cleavage of a large precursor protein; the peptide is natively unfolded but undergoes spontaneous self-association into dimers, trimers, soluble oligomers, and fibrils.[7] A third example is provided by Huntington's and related disorders. These diseases occur when a glutamine repeat domain in a protein is abnormally expanded, leading to aggregation, deposition, and tissue damage.[8,9]

Several kinetic models of protein aggregation have been described in the literature (see for example[10–14]). We have shown that mechanistic-based kinetic models can be reliably determined only if information on both aggregate molar concentration and aggregate size is obtained.[15] Yet, experimental investigation of protein aggregation processes is challenging. Aggregates are polydisperse in size, with a broad and possibly multimodal distribution. They can be morphologically complex. Preferably, one measures aggregation without labeling the protein, which can interfere with the aggregation process. Also of interest are methods that can be carried out *in situ*, in a variety of solvents, and over time.

A number of techniques have been used to measure aggregate concentration, size, and morphology. Size exclusion chromatography is useful for measuring the rate of monomer loss, but the method is insensitive to small quantities of

Correspondence concerning this article should be addressed to R. M. Murphy at regina@engr.wisc.edu.

aggregates, aggregates may adsorb to the column or be filtered in the frit, and dissociation of reversibly formed aggregates may occur.[16] Fluorescent dyes such as thioflavin T are frequently used to measure the mass concentration of fibrillar aggregates, but the minimum size for detecting aggregates is not well-established, non β-sheet aggregates are not detected, fluorescence can be affected by solvent conditions, and the fluorescence intensity is affected by fibril morphology and not necessarily linear in fibril mass.[17] Dye-binding assays are subject to a variety of interferences,[17] and do not provide any direct information about molar concentration, aggregate size, or aggregate morphology. Imaging techniques such as electron microscopy and atomic force microscopy are invaluable for qualitative work, but data are difficult to quantify, and surface effects may influence the observed size distribution.

Aggregate size can be measured rapidly and *in situ* using dynamic light scattering (DLS). Measurements are relatively fast (less than a minute in some cases is sufficient). The measured quantity is an autocorrelated intensity function, which is related to a mean diffusion coefficient, and, hence, a mean hydrodynamic radius. The size distribution can be inferred from analysis of the autocorrelation function using constrained regularization or other statistical techniques, but this is not always reliable. Moreover, DLS cannot report on the concentration of aggregates, in a sample that may contain unaggregated monomeric materials, small oligomers, and large aggregates. There are currently few experimental techniques that allow simultaneous measurement of protein aggregate size, size distribution, and number concentration.

Nanoparticle tracking (NTA) is a newer technique that holds promise for the study of amyloid fibril formation. Briefly, particles in the sample scatter light from an incident laser, and the scattered light is tracked using a CCD camera. The trajectory of the scattering particle is measured and its translational diffusion coefficient is calculated. The advantage of NTA is that individual particles are tracked, so that one obtains both a number concentration as well as a size distribution, not just a mean size. One disadvantage is that smaller particles are not easily measurable; the minimum size depends on the refractive index increment but for proteins this minimum size is around 30 nm. On the other side of the size spectrum, particles larger than $\sim$1 μm diffuse slowly and are challenging to measure accurately by NTA. Other techniques can both size and count particles, but they are best with larger particles. Flow imaging techniques use digital microscopy coupled with microfluidics to analyze particles in solution, but are limited to particle sizes of 1->50 μm dia.[18,19] Resonance mass measurement uses a cantilever with a microfluidic channel embedded on its surface to measure changes in the resonating frequency, which is proportional to the buoyant mass. This technique is best in the range of 0.5 to 2 μm.[20]

There are several recent studies in which NTA was used to detect and characterize protein aggregates arising during protein processing.[21,22] The technique has recently been used to characterize virus-containing preparations.[23] A few reports using NTA to characterize amyloid proteins are beginning to appear.[24–26] However, no quantitative assessment of its validity for characterization of amyloid protein samples has been reported to date. The objective of this work is to quantitatively assess NTA as a tool for investigating protein aggregation. We first validated NTA using latex beads; next we used DNA as a model of macromolecules with fibrillar morphology. Finally, we collected and evaluated NTA data for three aggregating protein systems. Our results are instructive in demonstrating some unique advantages as well as some limitations of single-particle diffusion measurements for investigating amyloid fibril formation.

Materials and Methods

Sample preparation

Nanosphere size standard (NIST Traceable Mean Diameter) polystyrene latex beads were purchased from Thermo Scientific (Fremont, CA) and used without further purification. Samples were prepared by diluting the beads into milliQ water.

Salmon DNA (Sigma) was diluted into Tris buffer (10 mM tris(hydroxymethyl)aminomethane, 100 mM EDTA, pH 8). Concentration was determined by absorbance at 260 nm; the 260/280 nm absorbance ratio was > 1.87, an indication that the sample is not contaminated with proteins. One sample was sonicated for 90 s to shear the DNA into smaller fragments. DNA size was determined by agarose gel electrophoresis. Linear polyethylenimine (MW 25 kDa) was generously donated by Dr. David Lynn.

Recombinant human TTR was produced and purified as described previously.[24] Proteins were further purified by size exclusion chromatography to remove trace amounts of aggregates. Stock solutions of TTR in phosphate-buffered saline (PBS:10 mM Na_2HPO_4/NaH_2PO_4 and 150 mM NaCl, pH 7.4) were diluted twofold into buffer (200 mM sodium acetate, 150 mM NaCl, pH 4.3) at 2 different concentrations (0.25 mg/mL and 0.35 mg/mL) to a final pH of 4.4 to initiate aggregation.

Lyophilized Aβ(1–40) (Anaspec, Inc.) was dissolved in 8M urea/0.01 M glycine-NaOH mixture (pH 10) to a final concentration of 2.8 mM, then snap-frozen, and stored at -80°C. Immediately before each experiment, frozen stocks were thawed and sonicated for 2 min before being diluted into PBSA (PBS with 0.02% sodium azide).

The peptide $K_2WQ_{24}K_2$ (Q24) was synthesized using standard Fmoc solid-phase methods on a Protein Technologies Symphony synthesizer. Glutamines with a trityl side chain protecting group, and lysines and tryptophan with a Boc side chain protecting group were purchased from Novabiochem (Gibbstown, NJ). Flanking lysine residues were added to increase solubility and tryptophan was used for concentration determination. The N-terminus was acetylated and the C-terminus was amidated to eliminate charge interactions of termini. Crude peptide was purified by reverse-phase HPLC. Peptide identity was confirmed by MALDI-TOF mass spectrometry (3833.95 Da measured; 3833.12 Da theoretical). Purified peptide stock solutions were made in water (adjusted with trifluoracetic acid to pH 3) and snap-frozen. To prepare samples, the stock solutions were thawed, filtered through 0.45 μm filter, and diluted into CHES buffer (10 mM N-cyclohexyl-2-aminoethanesulfonic acid, containing 140 mM NaCl, pH adjusted to 9).

Nanoparticle Tracking Analysis (NTA)

A Nanosight LM10 (Nanosight, Amesbury, UK) equipped with a 405 nm laser was used to collect NTA measurements. Samples for analysis were injected into the sample chamber using a syringe, and video capture was initiated immediately. For each experiment, one 30-s video was taken and analyzed using the NTA 2.3 software. All measurements were collected at room temperature with the camera level set to the maximum value, except for the 240 nm beads. All buffers

were filtered through 0.02 μm filters before use and checked for absence of scattering particles.

The particle size is reported as hydrodynamic radius R_h, determined by following the 2-D trajectory of each particle over a tracking time t [27,28]

$$\overline{(x,y)^2} = \frac{2kTt}{3R_h\eta} \quad (1)$$

where k = Boltzmann constant, T = temperature, and η = solvent viscosity. Particle size is reported to the nearest nm. Particle number concentration is calculated based on a scattering volume that is a function of instrument settings.

Dynamic Light Scattering (DLS). All buffers were filtered through 0.02 μm filters before use. Samples containing proteins were filtered through a 0.45 μm filter directly into a light-scattering cuvette and then placed into a bath of the index-matching solvent decahydronaphthalene with temperature controlled to 25°C. Data were collected at 90° scattering angle using a Brookhaven BI-200SM system (Brookhaven Instruments, Holtsville, NY) and an Innova 90C-5 argon laser (Coherent, Santa Clara, CA) operating at 488 nm and 150 mW. The autocorrelation function $g^{(1)}(\tau)$ was obtained as a function of the decay time τ and analyzed using the method of cumulants

$$\ln g^{(1)}(\tau) = -\Gamma_z\tau + \frac{1}{2}\mu_2\tau^2 \quad (2)$$

where the first cumulant $\Gamma_z = q^2\langle D\rangle_z$, q is the scattering vector (= 0.0242 nm in our experiment), and $\langle D\rangle_z$ is the apparent z-averaged (intensity-averaged) translational diffusion coefficient. $\langle D\rangle_z$ is converted to an apparent z-average hydrodynamic radius $\langle R_h\rangle_z$ using the Stokes–Einstein equation

$$\langle R_h\rangle_z = \frac{kT}{6\pi\eta\langle D\rangle_z} \quad (3)$$

Results and Discussion

Validation of NTA for particle sizing and particle counting with latex beads

We first prepared dilutions of 60 nm, 100 nm, and 240 nm beads (diameter, as certified by the manufacturer), and measured both the size and the particle number concentration by NTA. Dilutions were chosen based on maintaining 10–100 particles per viewing area, as recommended by the manufacturer. In all cases, the mean particle size was very close to that expected: 59 ± 3 nm for 60 nm beads, 99 ± 2 nm for 100 nm beads, and 239 ± 5 nm for 240 nm beads (mean $\pm$ SD from multiple repeat measurements).

We tested whether NTA was able to reliably measure distributions of mixtures of beads. 60 and 100 nm beads were mixed at a 1.2:1 number ratio. We were able to clearly detect a bimodal distribution, although the peak sizes were shifted slightly toward the center (64 and 96 nm, respectively) (Figure 1A). The measured number of 60 nm beads was about 15% lower than the number of 100 nm beads, even though the actual number of 60 nm beads was 20% higher. A similar phenomenon, but even more pronounced, was observed when 100 nm and 240 nm beads were mixed together at a 1:1 ratio. Again, the particle sizes were reasonably accurately determined, with a slight shift toward the center (Figure 1B), but the measured concentration for 100 nm beads was only about half that of the 240 nm beads. The much higher scattered intensity from the larger particles tends to obscure the presence of smaller particles and leads to undercounting.

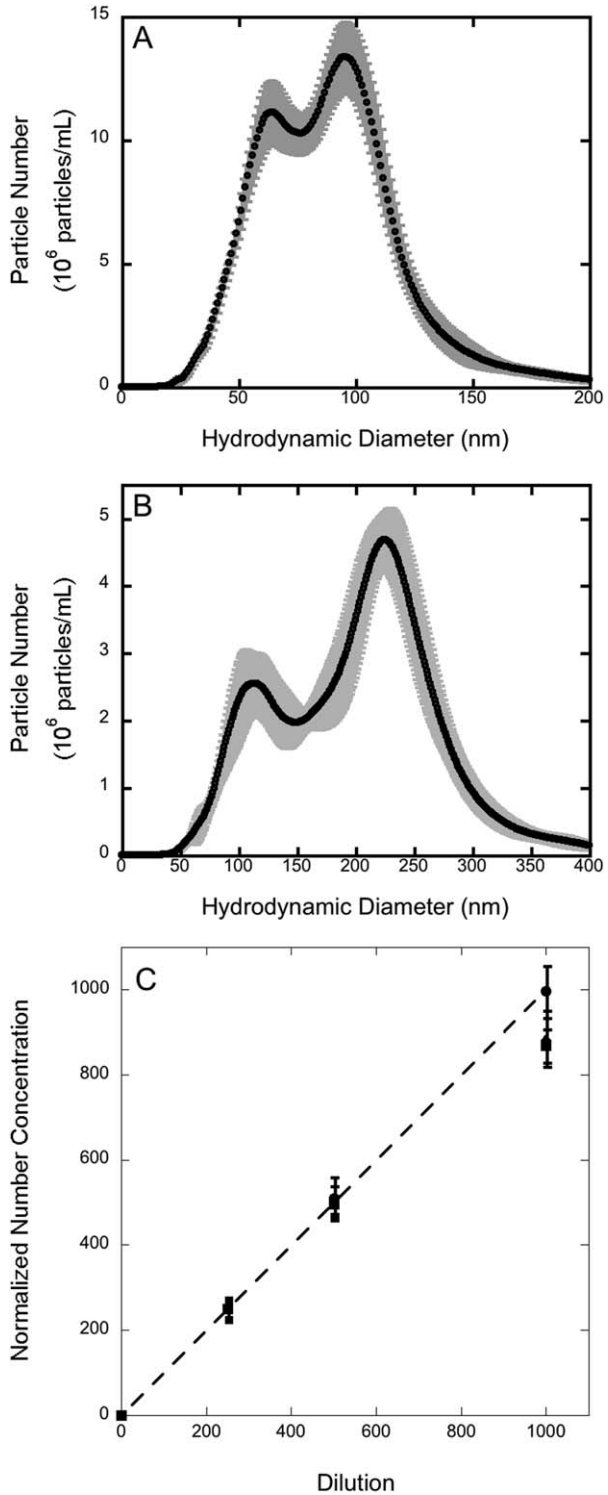

Figure 1. Validation of nanoparticle tracking analysis for polystyrene latex beads.

(A) Measured size distribution for a 1.2:1 mixture of 60 nm and 100 nm beads, (B) Measured size distribution for a 1:1 mixture of 100 nm and 240 nm beads, and (C) Relationship between particle count and dilution factor for 60 nm (•), 100 nm (■) and 240 nm (◆) beads. Data were normalized to 250 counts at the highest-dilution (lowest concentration) sample.

Table 1. Particle Number Concentration Measurements

Sample	Calculated (10^6 /mL)	Measured (10^6 /mL)	Ratio Measured/ Calculated
Latex Beads 60 nm	1000	1200±70	1.2
Latex Beads 100 nm	1000	1710±80	1.7
Latex Beads 240 nm	1000	1420±100	1.4
DNA 12 kb	34,000,000	1040±30	0.00003
DNA 12 kb + PEI	5600	266±12	0.048
DNA 12 kb, EMCCD	270,000	259	0.0096
DNA 12 kb + PEI, EMCCD	540	320	0.6

We next checked whether a linear response in particle count is obtained to dilution. For 60 nm beads, the measured concentration relative to the expected was highly linear, indicating excellent confidence in the relative number concentration (Figure 1C). Good results were obtained as long as the particles per viewing area were kept within the range recommended by the instrument manufacturer. For 100 nm and 240 nm beads, a modest deviation from linearity was observed at the highest concentration. These beads scatter very intensely, which appears to be the source of the deviation. This result suggests that more accurate number concentration counts for intense scatterers are best obtained at the lower end of range of particles per viewing area.

Finally, we examined the accuracy of the absolute particle number concentration determination. Latex particle samples were prepared by dilution from a 1 wt % solution as supplied from the manufacturer. We calculated the particle number concentration from the reported hydrodynamic diameter and density (1.05 g/mL), assuming spherical particles and accounting for the dilution factor. For all three particle sizes, the measured number concentration was ~20–70% higher than that calculated (Table 1). We suspect that much of the discrepancy results from systematic error in the wt % beads as supplied by the manufacturer, which is reported as an approximate concentration.

Several other groups have previously reported on the use of NTA to characterize size distributions and concentrations of polymeric beads, viruses, and other spherical particles. In general, and in agreement with our findings, both particle sizes and concentrations could be measured with reasonable accuracy, but with some caveats.[23,29–33]

Analysis of DNA by NTA

Latex particles are spherical polymeric materials, and we hypothesized that instrument performance might be different with particles of different shape or of biological origin. We chose DNA as a model system for analysis because (a) its large aspect ratio and semiflexible chain properties are similar to amyloid fibrils, and (b) relatively monodisperse samples in a range of lengths comparable to amyloid fibrils are commercially available.

Salmon DNA was used for these experiments. The sample was determined from agarose gel electrophoresis to be relatively monodisperse, with a size of 12.3 kb determined from calibrated standards (Figure 2A, insert). This size corresponds to a molecular weight $M = 8 \times 10^6$ Da and a contour length $L = 4100$ nm.[34] To convert this to an expected hydrodynamic radius R_h, we modeled DNA as a wormlike chain, assuming a chain diameter of 2.5 nm and a persistence length of 60 nm.[34–36] This yields an estimate of $R_h = 150$ nm. We prepared a second sample by sonication. By agarose gel electrophoresis we determined that the sonicated sample had a molecular weight distribution, ranging from 0.5 to 2 kb and centered around 1 kb (Figure 2B, insert); from this we calculated an estimate of $M = 0.7 \times 10^6$ Da, $L = 350$ nm, and $R_h = 30$ nm.

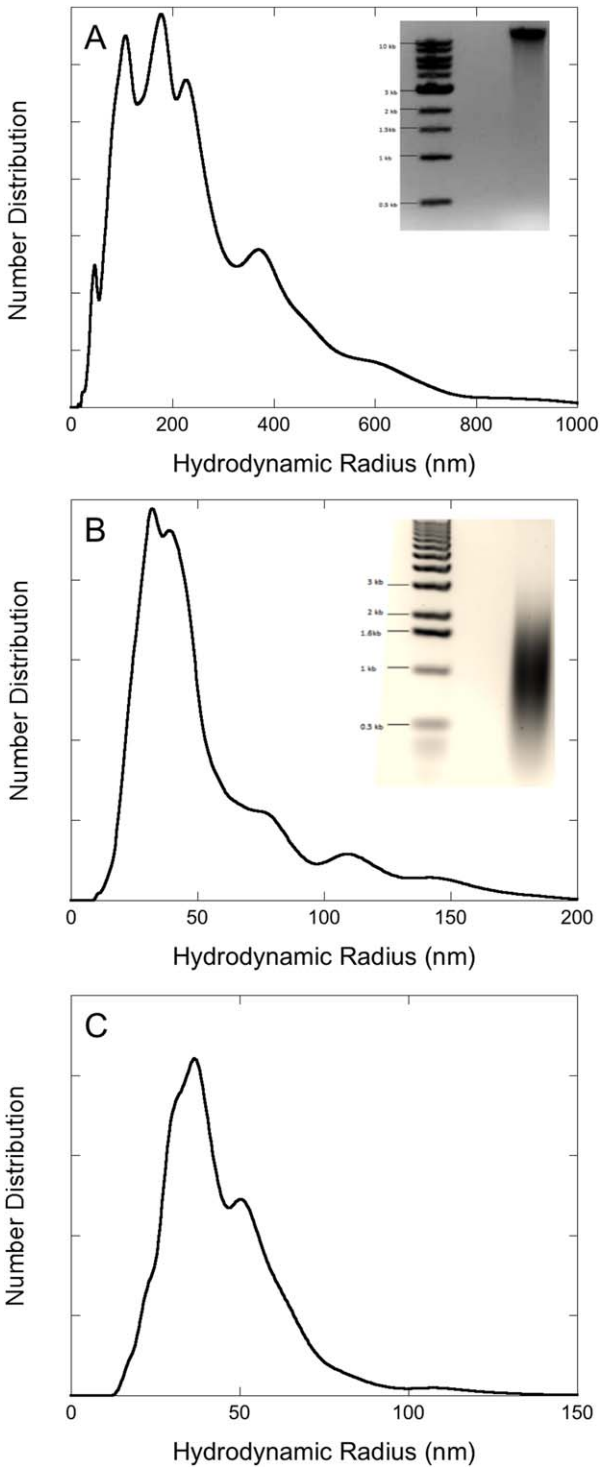

Figure 2. Nanoparticle tracking analysis of salmon DNA.

(A) Size distribution of 12 kb DNA, obtained by NTA. *Insert*, agarose gel electrophoresis analysis (B) size distribution of sonicated DNA, obtained by NTA. *Insert*, agarose gel electrophoresis analysis, and (C) size distribution of 12 kb DNA complexed with PEI. [Color figure can be viewed in the online issue, which is available at wileyonlinelibrary.com.]

The size distribution obtained for the DNA samples are shown in Figure 2A and 2B. Peaks in the distribution are at 178 nm (12 kb) and 32 nm (1 kb). These are about 10–15% larger than that calculated from the wormlike chain model; we consider this excellent agreement. The number-averaged mean R_h calculated from the distribution was 331 (12 kb) and 71 nm (1 kb). The size distribution was much broader for DNA than for latex particles, with a long tail toward larger hydrodynamic radii, particularly for the 12 kb sample. Size heterogeneity in the DNA sample is unlikely to fully account for the long tail: the agarose gel shows a relatively narrow band for the 12 kb sample. The anomalously slow diffusivity could be due to difficulties with particle centering and tracking.[27] Additionally, the 12 kb sample was prepared at 0.15 mg/mL, which happens to be the overlap concentration for DNA of this size.[37] At this concentration, entanglement effects may influence particle mobility.

We measured the accuracy of particle number concentration from DNA. We checked the particle number concentration versus dilution and found good linearity (data not shown), consistent with our experience with latex beads. We calculated the expected particle number concentration (particles per mL) from the mass concentration (measured by absorbance at 260 nm) and the molecular weight (known from agarose gel electrophoresis). We diluted sufficiently to obtain a particle number concentration in the desired range of about 10 to 100 particles in the viewing chamber. Surprisingly, the samples were nearly blank: we observed zero, one or two particles.

We, therefore, prepared samples at higher concentrations; these were the samples shown in Figures 2A and 2B. In sharp contrast to our result from latex particles, the particle number concentration was greatly underestimated by NTA (Table 1), by four orders of magnitude!

We hypothesized that the unexpectedly low-particle count was caused by low scattering intensity for DNA relative to its hydrodynamic size. The scattered intensity is a function of both the particle size and its composition, and there is a threshold of intensity below which particles will not be reliably detected.[28] The Nanosight LM10 instrument manufacturer reports that the minimum size detectable is ~10 nm dia. for gold nanoparticles and ~30 nm dia. for protein aggregates.

For point particles, the scattered intensity per particle I is proportional to the square of the molecular weight M and the square of the refractive index increment dn/dc

$$I \propto M^2 \left(\frac{dn}{dc}\right)^2 \tag{4}$$

dn/dc is a function of material properties as well as wavelength and temperature, and is approximately the same (~0.18 mL/g) for proteins and DNA.[38]

For particles that are larger than about 1/10 of the incident wavelength, an additional effect needs to be considered. Specifically, there can be multiple scattering centers that lead to interference effects that reduce the detected scattered intensity. This effect is quantified by the particle scattering factor $P(q)$

$$I \propto M^2 \left(\frac{dn}{dc}\right)^2 P(q) \tag{5}$$

$P(q)$ is a function of the scattering angle, particle shape, and particle characteristic dimensions. DNA is modeled as a semiflexible (wormlike) chain,[39,40] where

$$P(q) = \frac{2}{L_c{}^2} \int_0^{L_c} (L_c - t) \times \exp\left(-\frac{1}{6} q^2 l_k \times tf(t)\right) \times \frac{\sin(q \times tg(t))}{q \times tg(t)} dt \tag{6}$$

L_c is the contour length, and l_k is the Kuhn statistical segment length; for double-stranded DNA we used $l_k = 120$ nm, and $L_c = 335$ nm per kb.[36] The functions $tg(t)$ and $tf(t)$ are given elsewhere.[40] We calculated $P(q) = 0.06$ for 12 kb DNA, assuming a 90° scattering angle. (The actual scattering angle for the NTA ranges between 70 and 100° [28].) Because DNA is so long and thin, a solid sphere of equivalent M and a density of 1 g/mL would have $R_h = 15$ nm and $P(q) = 0.98$. In other words, the scattered intensity of a DNA particle with $R_h = 180$ nm is only ~6% of a sphere of similar M but $R_h = 15$ nm. Spherical protein particles of this size are at the threshold of detection of the NTA. Thus, DNA is a weak scatterer for its size, because its extended dimension leads to interference effects. We hypothesize that the effect of $P(q)$ is to decrease the scattered intensity of many DNA particles below the threshold of detection. This leads to the inability to detect many DNA particles, despite their large hydrodynamic size, and may explain the severe undercounting of DNA particles (Table 1).

To test this hypothesis, we mixed DNA with polyethyleneimine (PEI), a cationic polymer that binds to DNA and causes it to condense and collapse via charge neutralization. PEI alone ($M = 25$ kDa) was too small to be observed by NTA (data not shown). Assuming a 1:1 nitrogen: phosphate ratio in the PEI:DNA complex, we estimate the molecular weight of the complex to be ~13% larger than DNA alone. By itself, this increase in M would cause a small (~25%) increase in scattered intensity.

PEI-DNA complexes were significantly smaller than DNA alone (Figure 2C vs Figure 2A), with a peak in the distribution at $R_h = 36$ nm. This result indicates that DNA complexed to PEI is collapsed, as expected. The change in particle shape results in an increase in $P(q)$ to ~ 0.25. Based on $P(q)$ alone, the scattering intensity increases about fourfold, and so the particles that exceed the scattering threshold would increase, despite the smaller hydrodynamic size. This increase in scattered intensity proved to be very significant in placing DNA particles above the detection threshold: we saw a ~ 1500-fold improvement in capturing the number of particles (Table 1). The measured particle concentration was still ~ 20-fold below that expected, however.

We conclude from this analysis that NTA can successfully measure the hydrodynamic size of long semiflexible macromolecules such as DNA. Caution must be exercised in interpreting any long tail, as this could be due to technical problems with particle tracking, or to entanglement effects. More critically, measurement of the particle number concentration is fraught with difficulties that we believe are due to weak scattering intensities compared to beads of equivalent molecular weight, because of the extended shape of the particles. Much higher sensitivity in detection is necessary. We recently installed a high-sensitivity EMCCD camera and re-examined DNA samples, without or with PEI. The higher sensitivity resulted in approximately 10-fold to 30-fold increase in particle detection (Table 1), and much better detection of particles in the ~ 50 nm size range (not shown). We are currently working on methods to further improve detection of these samples.

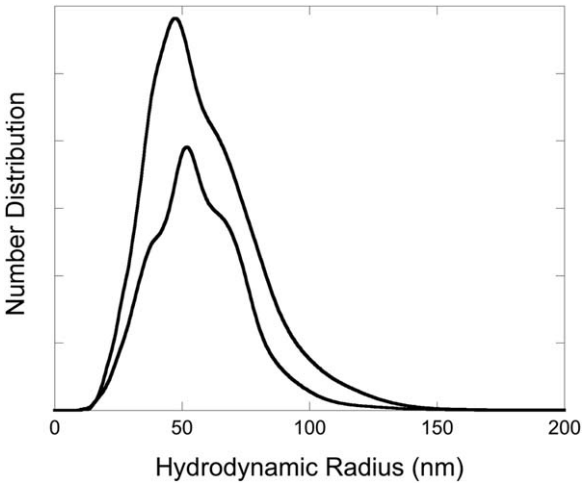

Figure 3. Size distributions obtained after acid-induced aggregation of TTR, obtained by nanoparticle tracking.

The data were collected immediately after dilution into buffer at pH 4.4. Distributions at 0.25 mg/mL (lower) and 0.35 mg/mL (upper) were measured.

Analysis of amyloidogenic proteins by NTA

We next evaluated three different amyloid protein systems using NTA. Each of these systems was used to investigate a different aspect of NTA.

Aggregate Size Distribution and Concentration. Transthyretin (TTR) is a 56 kDa homotetrameric protein that serves as a transport protein in plasma and cerebrospinal fluid. It is a highly stable folded protein at physiological pH, but exposure to low pH (4–5) induces fibril formation. The process is believed to progress via dissociation of the tetramer to monomer, modest conformational rearrangement in the monomer, and then reassociation of the monomer into fibrils.[41]

We examined acid-induced aggregation of TTR using NTA, and compared our data to dynamic light scattering (DLS) analysis. Data were collected at two concentrations (0.25 and 0.35 mg/mL, corresponding to typical concentrations in the plasma) immediately after dilution into the low pH buffer.

Particle-size distributions were fairly broad, but more symmetrical than those for DNA, and were very similar at the two concentrations (Figure 3). The number-averaged R_h calculated from the distribution was similar for both concentrations: 58 nm at 0.25 mg/mL, and 60 nm at 0.35 mg/mL. The measured particle concentration increased from 630 million particles per mL at 0.25 mg/mL to 1050 million particles per mL at 0.35 mg/mL. The 65% greater number of particles at a 40% higher total protein concentration is reasonable and consistent with previously reported second-order reaction rate.[42]

We analyzed similarly prepared samples by DLS, and obtained measurements of $<R_h>_z = 30$ nm (0.25 mg/mL) and 43 nm (0.35 mg/mL). These sizes are significantly smaller than those obtained from NTA. There are two important differences between NTA and DLS measurements. First, the average hydrodynamic radius for NTA is averaged over the number of particles, whereas the DLS average is intensity, or "z" averaged. This effect yields larger sizes for DLS than for NTA. Second, unaggregated TTR ($R_h = 3.5$ nm) contributes to the DLS signal but is too small to be detected by NTA. This effect reduces the measured mean size for DLS compared to NTA. Since $<R_h>_{z,DLS} < <R_h>_{z,NTA}$, the latter effect is likely to be important.

To calculate a z-average R_h from the NTA size distribution, we used

$$\left[\frac{\sum N_i M_i^2 P(q)_i / R_{h,i}}{\sum N_i M_i^2 P(q)_i}\right]^{-1} = \langle R_h \rangle_{z,NTA} \tag{7}$$

where N_i = the number concentration, M_i is the molecular weight, and $P(q)_i$ is the particle shape factor, of aggregates of size i. The summation is taken over all aggregates. N_i and $R_{h,i}$ were taken directly from the NTA data, and we calculated M_i, and $P(q)_i$ by modeling TTR aggregates as stiff fibrils of 8 nm diameter and 500 nm persistence length. Fibril diameter is based on EM images.[43] TTR fibrils in EM images are long and relatively stiff, with little curvature, and our results were not sensitive to the assumed persistence length within the range of 150–1000 nm. With this analysis, we calculated $<R_h>_{z,NTA} = 60$ nm and 62 nm for 0.25 and 0.35 mg/mL, respectively.

The DLS data, unlike NTA, includes contributions from unaggregated protein: we used the equation

$$\left[\frac{\sum N_i M_i^2 P(q)_i / R_{h,i} + N_m M_m^2 / R_{h,m}}{\sum N_i M_i^2 P(q)_i + N_m M_m^2}\right]^{-1} = \langle R_h \rangle_{z,DLS} \tag{8}$$

where N_m, M_m and $R_{h,m}$ are the number concentration, molecular weight (56 kDa), and hydrodynamic radius (3.5 nm), respectively, of unaggregated TTR. The weight fraction of protein in aggregated form w_{agg} is

$$w_{agg} = \frac{\sum N_i M_i}{\sum N_i M_i + N_m M_m} \tag{9}$$

where the summation is taken over all aggregates.

Using Eq. 6–9, and the combined analysis from NTA and DLS, we solved for $w_{agg.}$ We calculated that 10 wt % of TTR at 0.25 mg/mL and 21 wt % at 0.35 mg/mL is incorporated into aggregates. As a comparison, we prepared TTR at pH 4.4 and 0.35 mg/mL and estimated the fraction of aggregated protein by two methods: filtration (0.22 μM filter) and centrifugation. 15–25 wt % of the material was retained (compared to 0% for TTR at neutral pH). This is in good agreement with the 21 wt % estimate obtained by comparing DLS and NTA data.

As described earlier, we observed many fewer particles in DNA samples than expected. We wondered if this were true for TTR aggregates also. Using the absolute number concentration obtained from NTA, we estimated that only ~0.01 wt % of the TTR was aggregated. This is about 1000-fold lower than estimates obtained above by either direct experiment (filtration or sedimentation), or by combined analysis of NTA+DLS data. We believe that this result is due to severe undercounting of fibrillar aggregates due to their relatively low-scattering cross section compared to their size, because of their extended shape. This is the similar effect as that observed for DNA. We conclude that, for amyloid fibrils, NTA measurements of fibril size are reliable, but measurements of fibril concentration are not. However, by combining NTA with DLS data, meaningful concentration information is obtained.

Aggregation kinetic

Beta-amyloid (Aβ) is a 4 kDa peptide released by proteolysis from a cell membrane-associated precursor protein. As a

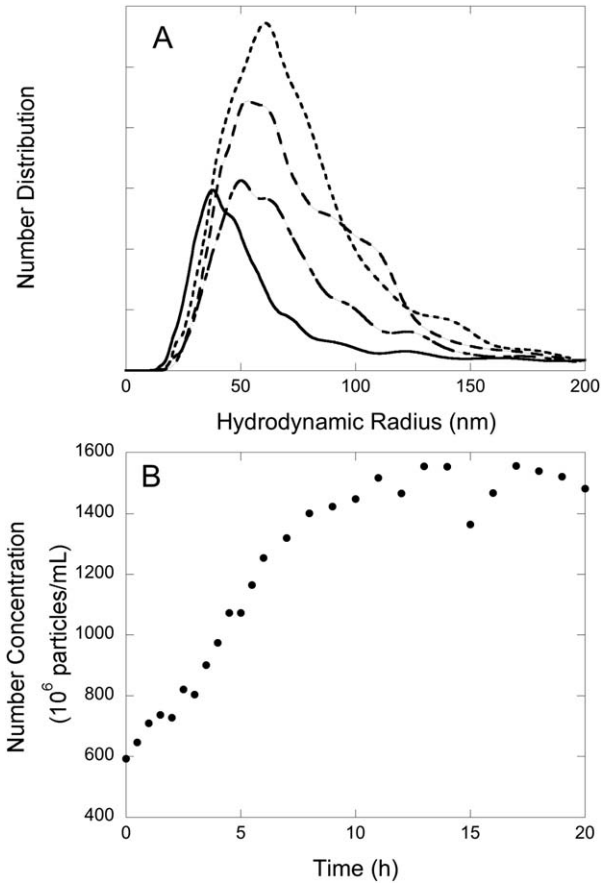

Figure 4. Aβ was prepared in PBS at 0.12 mg/mL, and its aggregation was followed over time by nanoparticle tracking.

(A) Aβ size distribution versus time. Data shown were taken at 0 h (solid), 3 h (long dash), 6 h (medium dash), and 10 h (short dash) after initial sample preparation, and (B) measured particle number concentration of Aβ aggregates vs. time.

monomer, it is disordered and lacks any regular secondary structure or fold, but it spontaneously self-assembles into multimers, oligomers, and large fibrillar aggregates. Deposition of Aβ fibrils is one of the major pathological markers of Alzheimer's disease; it is widely believed that soluble oligomeric intermediates rather than mature fibrils are toxic to neurons.[7]

For aggregating systems, we are frequently interested not only in characterizing the aggregation state at a given time, but the rate and pattern of growth. This is especially important for systems such as Aβ, where kinetic intermediates are likely to be the most toxic species. If it is possible to follow protein aggregation over longer periods of time, then NTA could be a very useful tool for developing kinetic models, because of the potential to measure simultaneously both size distribution and particle number over time.

To test the feasibility of using NTA to monitor aggregation kinetics, we prepared Aβ at 0.12 mg/mL. We were able to collect data over several hours. We observed a size distribution that became broader over time, with a shift toward larger particles (Figure 4A). The measured particle concentration also increased with time (Figure 4B). This result demonstrates that aggregation involves both the formation of new aggregates and the increase in size of pre-existing aggregates. Such a distinction could not be made from DLS data alone; this example demonstrates the power of NTA to help distinguish among different mechanisms of aggregate growth. In work published elsewhere, NTA was used in combination with other techniques to explore mechanisms of inhibition of Aβ aggregation.[24]

With Aβ, as with DNA and TTR, we observed a large discrepancy between the particle concentration as measured by NTA, and that calculated by other means. We believe that the measured particle concentrations can be taken only as relative rather than absolute. Further progress on overcoming this limitation is needed to take full advantage of the potential of NTA to tease out fully quantitative data for modeling aggregation kinetics.

Differences in aggregate structure

Huntington's disease and several related disorders are caused by abnormal expansion of a glutamine repeat domain in the associated protein. We synthesized a peptide containing a repeat domain of 24 glutamines (Q24) as a model of proteins containing glutamine repeats. Monomeric Q24 lacks regular secondary structure, but spontaneously self-associates into large aggregates with a fibrillar morphology.[44]

Q24 was diluted into buffer at pH 9 to trigger aggregation, and NTA data were collected immediately after dilution. The size distribution was similar at the two concentrations tested (Figure 5). Compared to TTR (Figure 3) or early Aβ aggregates (Figure 4A), Q24 aggregates were larger, and the size distribution was broader, with a broad peak from about 70 to 110 nm at 0.038 mg/mL and from about 80 to 120 nm at 0.076 mg/mL.

All proteins carry some waters of hydration but for the most part, water is excluded from the interior of a folded protein, and hydrogen bond potential of the backbone amides is satisfied largely through protein-protein rather than protein-solvent interactions. Mature amyloid fibrils are similarly dehydrated, and water (and its removal) plays a critical role in protein aggregation and amyloid structure formation.[45] We hypothesize that, unlike folded proteins or mature amyloid fibrils, Q24 aggregates contain a large amount of associated waters. The glutamine side chain is an amide,

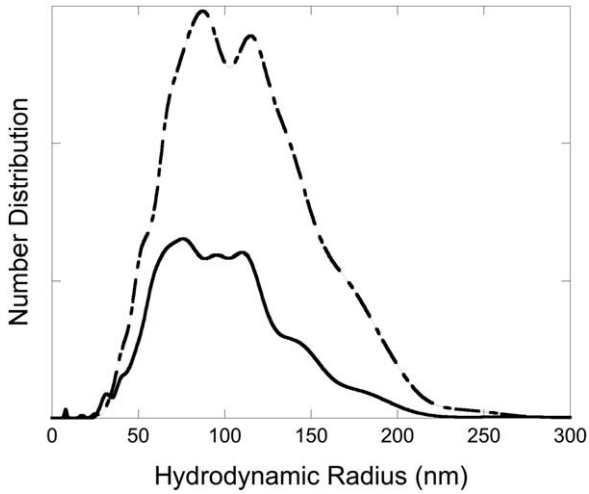

Figure 5. Size distributions of Q24 aggregates, obtained by nanoparticle tracking.

Stock solutions of Q24 were diluted into buffer at pH 9 to initiate aggregation. Peptide concentrations were 0.038 mg/mL (solid) and 0.076 mg/mL (dashed).

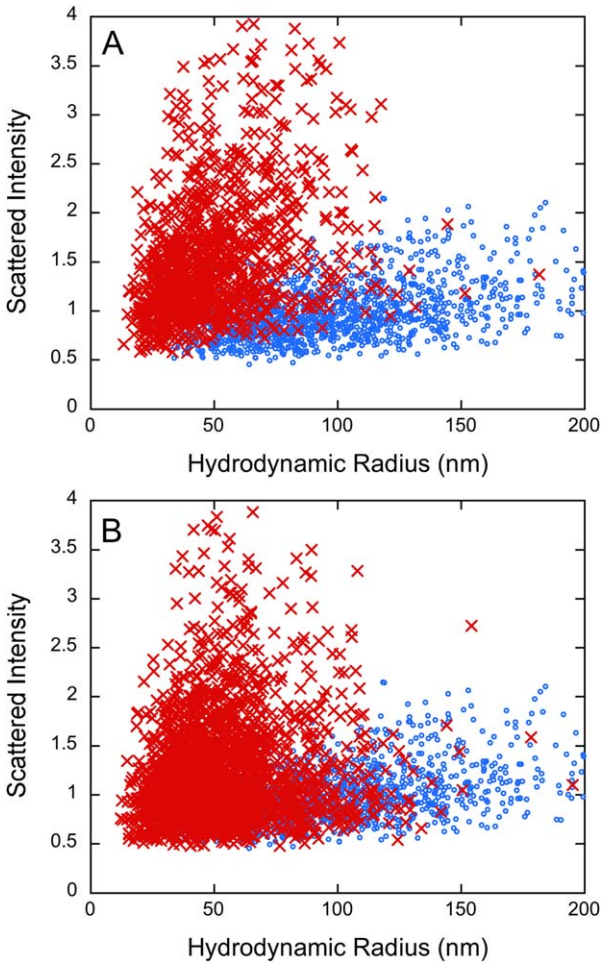

Figure 6. Relationship between hydrodynamic radius and scattering intensity of individual particles.

(A) Comparison of Q24 (blue) with Aβ (red), and (B) comparison of Q24 (blue) with N24 (red). Data were taken with identical camera settings and comparable particle counts.

[Color figure can be viewed in the online issue, which is available at wileyonlinelibrary.com]

capable of participating in hydrogen bond formation as both donor and acceptor, and glutamine is considered to be a polar amino acid. We previously showed, using quartz crystal microbalance and optical waveguide light-mode spectroscopy,[46] that as much as 40–70% of the material in polyQ aggregates might be water. Within this context it is interesting to note an early interpretation of X-ray diffraction data that amyloid fibrils are "water-filled nanotubes", [47] although this conclusion has been challenged by others.[48]

If Q24 aggregates are indeed "water-logged", they would be hydrodynamically large particles but the associated waters would not contribute to excess scattering over buffer. If true, we should be able to detect this from nanoparticle tracking data, by comparing the intensity of Q24 aggregates to those of more "folded" fibrils: particles of Q24 should scatter less light than particles of identical hydrodynamic size but greater dehydration. This is possible with NTA, because individual particles are counted, and both hydrodynamic size and scattered intensity are recorded for each particle. The idea of using different scattering intensities to distinguish particles of different materials has been suggested [28], but not for different kinds of protein aggregates.

We plotted the normalized scattered intensity versus particle size for every counted particle, and compared Q24 to Aβ (Figure 6A). We observed clear segregation into two separate clusters, with aggregates of Q24 scattering less light than Aβ aggregates of equal size, consistent with the hypothesis that Q24 aggregates contain more water and are less "folded" than Aβ aggregates.

To further explore this idea, we synthesized a peptide, N24, containing an asparagine repeat domain. The side chain of asparagine, like glutamine, is an amide, but asparagine's side chain is one $-CH_2-$ group shorter. The difference in side chain length changes the ability to form "tight" fibrillar aggregates, and N-rich peptides more readily form highly structured fibrils than Q-rich peptides.[49] We compared NTA data for N24 to Q24 (Figure 6B) and observed that scattered intensity was higher for N24 particles than for Q24, at equivalent size. This result is consistent with the hypothesis that polyasparagine fibrils are more highly structured than polyglutamine fibrils. Closer examination reveals that there may be two clusters of N24 aggregates, a smaller one that overlaps with Q24 and a larger cluster where the particles have higher scattered intensity. We speculate that these clusters may be diagnostic of polymorphism in N24 aggregates.

This result, although very preliminary, suggests a unique and powerful advantage of NTA for studying protein aggregation: not only could one rapidly determine, *in situ*, the size of protein aggregates, but also obtain information about their structure!

Conclusions

Nanoparticle tracking analysis is a relatively new technique that shows great promise for use in studies of protein aggregation kinetics and mechanisms. Reasonably accurate measures of size distributions can be obtained rapidly, without labeling, in the buffer of choice. A potential important advantage of NTA over DLS and other techniques is the ability to directly measure particle number concentration. This is a key measure needed for kinetic modeling. We found that particle numbers were reliable for spherical latex beads but were greatly underestimated for DNA and for fibrillar aggregates. We attribute this finding to the weak scattering from particles with extended morphology. Overcoming this problem may require use of much more sensitive detectors. The unique ability of NTA to measure both size and scattering intensity of individual particles opens up a powerful new application of the technique: to rapidly and directly obtain information about the compactness and extent of hydration of protein aggregates. With further validation and development of the technique, NTA could yield a treasure trove of insight into protein aggregation mechanisms.

Acknowledgments

This work was supported by grant R01AG033493 from National Institutes of Health, and grant CBET-1262729 from National Science Foundation.

Literature Cited

1. Murphy RM. Peptide aggregation in neurodegenerative disease. *Annu Rev Biomed Eng*. 2002;4:155–174.
2. Tycko R, Wickner RB. Molecular structures of amyloid and prion fibrils: Consensus versus controversy. *Accounts Chem Res*. 2013;46: 1487–1496.

3. Lotz GP, Legleiter J. The role of amyloidogenic protein oligomerization in neurodegenerative disease. *J Mol Med*. 2013;91:653–664.
4. Wetzel R. Kinetics and thermodynamics of amyloid fibril assembly. *Accounts Chem Res*. 2006;39:671–679.
5. Westermark P, Sletten K, Johansson B, Cornwell GG. Fibril in senile systemic amyloidosis is derived from normal transthyretin. *Proc Natl Acad Sci USA*. 1990;87:2843–2845.
6. Hou X, Aguilar MI, Small DH. Transthyretin and familial amyloidotic polyneuropathy - Recent progress in understanding the molecular mechanism of neurodegeneration. *FEBS J*. 2007;274:1637–1650.
7. Haass C, Selkoe DJ. Soluble protein oligomers in neurodegeneration: lessons from the Alzheimer's amyloid beta-peptide. *Nat Rev Mol Cell Bio*. 2007; 8:101–112.
8. Bates G. Huntingtin aggregation and toxicity in Huntington's disease. *Lancet*. 2003;361:1642–1644.
9. Gusella JF, MacDonald ME. Molecular genetics: Unmasking polyglutamine triggers in neurodegenerative disease. *Nat Rev Neurosci*. 2000;1:109–115.
10. Li Y, Roberts CJ. Lumry-Eyring nucleated-polymerization model of protein aggregation kinetics. 2. Competing growth via condensation and chain polymerization. *J Phys Chem B*. 2009;113:7020–7032.
11. Andrews JM, Roberts CJ. A Lumry-Eyring nucleated polymerization model of protein aggregation kinetics: 1. Aggregation with preequilibrated unfolding. *J Phys Chem B*. 2007;111:7897–7913.
12. Morris AM, Watzky MA, Finke RG. Protein aggregation kinetics, mechanism, and curve-fitting: A review of the literature. *BBA-Proteins Proteom*. 2009;1794:375–397.
13. Pallitto MM, Murphy RM. A mathematical model of the kinetics of beta-amyloid fibril growth from the denatured state. *Biophys J*. 2001;81:1805–1822.
14. Cohen SIA, Vendruscolo M, Welland ME, Dobson CM, Terentjev EM, Knowles TPJ. Nucleated polymerization with secondary pathways. I. Time evolution of the principal moments. *J Chem Phys*. 2011;135:065105.
15. Bernacki JP, Murphy RM. Model discrimination and mechanistic interpretation of kinetic data in protein aggregation studies. *Biophys J*. 2009;96:2871–2887.
16. Carpenter JF, Randolph TW, Jiskoot W, Crommelin DJA, Middaugh CR, Winter G. Potential inaccurate quantitation and sizing of protein aggregates by size exclusion chromatography: Essential need to use orthogonal methods to assure the quality of therapeutic protein products. *J Pharm Sci*. 2010;99:2200–2208.
17. Jameson LP, Smith NW, Dzyuba SV. Dye-binding assays for evaluation of the effects of small molecule inhibitors on amyloid (Abeta) self-assembly. *ACS Chem Neurosci*. 2012;3:807–819.
18. Sharma DK, King D, Oma P, Merchant C. Micro-flow imaging: Flow microscopy applied to sub-visible particulate analysis in protein formulations. *AAPS J*. 2010;12:455–464.
19. Zolls S, Tantipolphan R, Wiggenhorn M et al. Particles in therapeutic protein formulations, Part 1: Overview of analytical methods. *J Pharm Sci*. 2012;101:914–935.
20. Weinbuch D, Zolls S, Wiggenhorn M, Friess W, Winter G, Jiskoot W, Hawe A. Micro-flow imaging and resonant mass measurement (Archimedes) - complementary methods to quantitatively differentiate protein particles and silicone oil droplets. *J Pharm Sci*. 2013; 102:2152–2165.
21. Bai SJ, Murugesan Y, Vlasic M, Karpes LB, Brader ML. Effects of submicron particles on formation of micron-sized particles during long-term storage of an interferon-beta-1a solution. *J Pharm Sci*. 2013;102:347–351.
22. Filipe V, Kukrer B, Hawe A, Jiskoot W. Transient molten globules and metastable aggregates induced by brief exposure of a monoclonal IgG to low pH. *J Pharm Sci*. 2012;101:2327–2339.
23. Kramberger P, Ciringer M, Strancar A, Peterka M. Evaluation of nanoparticle tracking analysis for total virus particle determination. *Virol J*. 2012;9.
24. Yang DT, Joshi G, Cho PY, Johnson JA, Murphy RM. Transthyretin as both a sensor and a scavenger of beta-amyloid oligomers. *Biochemistry*. 2013;52:2849–2861.
25. Dubnovitsky A, Sandberg A, Rahman MM, Benilova I, Lendel C, Hard T. Amyloid-beta protofibrils: Size, morphology and synaptotoxicity of an engineered mimic. *PLoS One*. 2013;8:e66101.
26. Torosantucci R, Weinbuch D, Klem R, Jiskoot W. Triethylenetetramine prevents insulin aggregation and fragmentation during copper catalyzed oxidation. *Eur J Pharm Biopharm*. 2013;84:464–471.
27. Malloy A, Carr B. Nanoparticle tracking analysis - the halo (TM) system. *Part Part Syst Char*. 2006;23:197–204.
28. Gallego-Urrea JA, Tuoriniemi J, Hassellov M. Applications of particle-tracking analysis to the determination of size distributions and concentrations of nanoparticles in environmental, biological and food samples. *Trac Trend Anal Chem*. 2011;30:473–483.
29. Dragovic RA, Gardiner C, Brooks AS, Tannetta DS, Ferguson DJP, Hole P, Carr B, Redman CWG, Harris AL, Dobson PJ, Harrison P, Sargent IL. Sizing and phenotyping of cellular vesicles using nanoparticle tracking analysis. *Nanomed Nanotechnol*. 2011;7:780–788.
30. Du SF, Kendall K, Morris S, Sweet C. Measuring number-concentrations of nanoparticles and viruses in liquids on-line. *J Chem Technol Biot*. 2010;85:1223–1228.
31. Boyd RD, Pichaimuthu SK, Cuenat A. New approach to inter-technique comparisons for nanoparticle size measurements; using atomic force microscopy, nanoparticle tracking analysis and dynamic light scattering. *Colloid Surface A*. 2011;387:35–42.
32. Filipe V, Hawe A, Jiskoot W. Critical evaluation of nanoparticle tracking analysis (nta) by nanosight for the measurement of nanoparticles and protein aggregates. *Pharm Res Dordr*. 2010;27:796–810.
33. Anderson W, Kozak D, Coleman VA, Jamting AK, Trau M. A comparative study of submicron particle sizing platforms: Accuracy, precision and resolution analysis of polydisperse particle size distributions. *J Colloid Interf Sci*. 2013;405:322–330.
34. Amoros D, Ortega A, de la Torre JG. Hydrodynamic properties of wormlike macromolecules: Monte Carlo simulation and global analysis of experimental data. *Macromolecules*. 2011;44:5788–5797.
35. Yamakawa H, Fujii M. Translational friction coefficient of wormlike chains. *Macromolecules*. 1973;6:407–415.
36. Godfrey JE, Eisenberg H. Flexibility of low-molecular weight double-stranded DNA as a function of length.2. Light-scattering measurements and estimation of persistence lengths from light-scattering, sedimentation and viscosity. *Biophys Chem*. 1976;5:301–318.
37. Hur JS, Shaqfeh ESG, Babcock HP, Smith DE, Chu S. Dynamics of dilute and semidilute DNA solutions in the start-up of shear flow. *J Rheol*. 2001; 45:421–450.
38. Huglin MB. Specific refractive index increments of polymer solutions.I. Literature values. *J Appl Polym Sci*. 1965;9:3963.
39. Koyama R. Light-scattering of stiff chain polymers. *J Phys Soc Jpn*. 1973;34:1029–1038.
40. Shen CL, Fitzgerald MC, Murphy RM. Effect of acid predissolution on fibril size and fibril flexibility of synthetic beta-amyloid peptide. *Biophys J*. 1994;67:1238–1246.
41. Foss TR, Wiseman RL, Kelly JW. The pathway by which the tetrameric protein transthyretin dissociates. *Biochemistry*. 2005;44:15525–15533.
42. Hurshman AR, White JT, Powers ET, Kelly JW. Transthyretin aggregation under partially denaturing conditions is a downhill polymerization. *Biochemistry*. 2004;43:7365–7381.
43. Cardoso I, Goldsbury CS, Muller SA, Olivieri V, Wirtz S, Damas AM, Aebi U, Saraiva MJ. Transthyretin fibrillogenesis entails the assembly of monomers: A molecular model for in vitro assembled transthyretin amyloid-like fibrils. *J Mol Biol*. 2002;317:683–695.
44. Walters RH, Murphy RM. Examining polyglutamine peptide length: A connection between collapsed conformations and increased aggregation. *J Mol Biol*. 2009;393:978–992.
45. Thirumalai D, Reddy G, Straub JE. Role of water in protein aggregation and amyloid polymorphism. *Accounts Chem Res*. 2012;45:83–92.
46. Walters RH, Jacobson KH, Pedersen JA, Murphy RM. Elongation kinetics of polyglutamine peptide fibrils: A quartz crystal microbalance with dissipation study. *J Mol Biol*. 2012;421:329–347.
47. Perutz MF, Finch JT, Berriman J, Lesk A. Amyloid fibers are water-filled nanotubes. *Proc Natl Acad Sci USA*. 2002;99:5591–5595.
48. Sikorski P, Atkins E. New model for crystalline polyglutamine assemblies and their connection with amyloid fibrils. *Biomacromolecules*. 2005;6:425–432.
49. Halfmann R, Alberti S, Krishnan R, et al. Opposing effects of glutamine and asparagine govern prion formation by intrinsically disordered proteins. *Mol Cell*. 2011;43:72–84.

Manuscript received Dec. 16, 2013.